Journal of the European Ceramic Society **18** (1998) 1373–1379

PII: S0955-2219(98)00067-3
0955-2219/98/$—see front matter

Influence of Fe^{3+} on Sintering and Microstructural Evolution of Reaction Sintered Calcium Hexaluminate

Cristina Domínguez* and Ramón Torrecillas

Instituto Nacional del Carbón, CSIC, Ap. 73, 33080 Oviedo, Spain

Abstract

The phase evolution during reaction sintering of stoichiometric mixtures of $CaCO_3/(6-x)Al_2O_3/xFe_2O_3$ was investigated. The microstructural evolution as a function of iron content and firing temperature was also studied. It was found that the appearance during sintering of several intermediate phases (CA, CA, and CAF_2) as well as the phase evolution during the $CaO{\cdot}6(Al,Fe)_2O_3$ solid solution formation and the final microstructures after sintering, can be explained by means of the $CaO–Al_2O_3–Fe_2O_3$ phase equilibrium diagram. © *1998 Elsevier Science Limited. All rights reserved*

1 Introduction

The $CaO–Al_2O_3$ system was studied in detail due to its importance in the steel, cement and ceramic industries.[1,2] It contains a number of stable intermediate compounds: C_3A, $C_{12}A_7$, CA, CA_2 and CA_6, of which the last one is the richest in alumina. Calcium hexaluminate, or hibonite, is stable up to the peritectic point, 1875°C. At this temperature, it decomposes, giving alumina and a glassy phase. The compound formulation used is conventional cement notation, i.e. $C=CaO$, $A=Al_2O_3$, $F=Fe_2O_3$, thus $CA_6=CaO{\cdot}6Al_2O_3$, etc.

CA_6 crystallises in the hexagonal system, space-group $P6_3/mmc$, and presents the structure of magnetoplumbite (Fig. 1). This structure is composed of 'spinel blocks' and 'conduction layers', which are stacked alternately to form a sort of layer structure.[3–6] Spinel blocks are composed only of Al^{3+} and O^{2-} ions, and have the same rigid structure as spinel. Large cations such as Ca^{2+} are usually located in the spacious conduction layer, which has a mirror symmetry plane.

The morphology of CA_6 crystals or grains shows preferential growth along their basal plane. This growth-rate anisotropy gives them platelike morphologies, but preliminary studies revealed that the morphology of the CA_6 grains could be readily changed (from platelet to equiaxed) by modifying the processing conditions.[7–9]

Calcium hexaluminate forms extensive range of solid solution in the $CaO–Al_2O_3–Fe_2O_3$ system.[10–13] The solid solution mechanism has been shown to be the replacement of Al^{3+} by Fe^{3+} in the CA_6 lattice, which means that the range of CA_6 solid solution compositions lie along the join line $CA_6–CF_6$, as shown in Fig. 2. CF_6 is not a real phase, and for this reason it has not been presented in the figure.

CA_6 presents a large primary crystallisation field in the $CaO–Al_2O_3–Fe_2O_3$ system, which means low solubility in iron oxides containing slags. It is also highly stable in reducing atmospheres.[14] These properties allow CA_6 to be in contact with steel and iron at high temperature without significant corrosion of the ceramic material, making calcium hexaluminate a potentially suitable material as refractory for the iron and steel industries. CA_6 has a coefficient of thermal expansion close to alumina ($8–8{\cdot}5\times10^{-6}\ °C^{-1}$)[15–17] and a lower density ($3{\cdot}79\ g/cm^3$),[18] which in addition to this particular microstructure, gives CA_6 improved thermal shock behaviour, one of the main problems of alumina.

Recently there has been a renewed interest in the processing of ceramics whose microstructure exhibits platelike grain morphologies. This has arisen in great part due to the fact that elongated grains can act as bridging sites in the wake of a crack, hence resulting in improved mechanical behaviour. Between magnetoplumbites that present this kind of morphology, hibonite has been chosen as a reinforcing material in alumina composites[19–22] due to both its mechanical and thermal expansion properties. Calcium hexaluminate is also starting to be used as alumina fibre coatings.[23,24] Due to its

*To whom correspondence should be addressed.

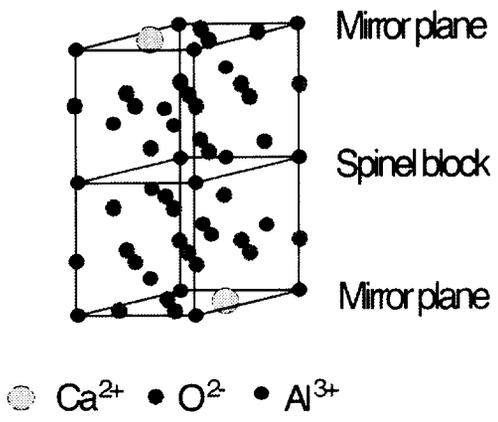

Fig. 1. Magnetoplumbite structure.

easy cleaving crystallographic basal planes oriented parallel to the fibre–matrix interface, this interface is sufficiently weak to deflect cracks, therefore toughening the composite, and strong enough that such transverse strengths are not too low.

Magnetoplumbites are used as nuclear waste containers[25–28] because ions in the mirror plane region between the spinel blocks are essentially immobile. For this reason they are good host structures for fission products such as Sr, Ba, Cs, and Ce for very long-term immobilisation.

In the past few years, CA_6–CF_6 solid solution compounds have been of interest due to their specific magnetic behaviour and electronic conduction. CA_6 is diamagnetic and a gradual increase in the magnetic susceptibility has been found up to the limit of the solid solution series, while a great increase in the susceptibility has been found with higher CF_6 content, inhomogeneous compounds.[29–32]

The powder synthesis, sintering, thermal stability and lately mechanical properties of pure CA_6 have been studied; however, there are no reports about the influence of Fe_2O_3 in the sintering behaviour and microstructure of calcium hexaluminate.

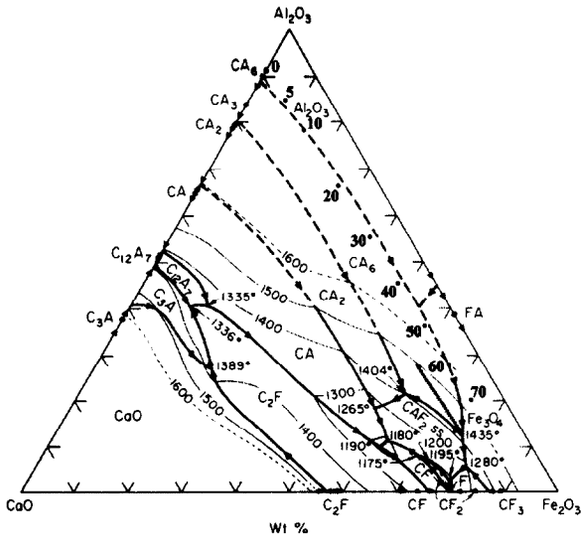

Fig. 2. CaO–$Al_2O_3Fe_2O_3$ phase diagram.

2 Experimental Procedure

2.1 Processing

Alumina (CT3000SG, ALCOA, Germany), calcium carbonate (ASTURCAL, Spain) and hematite (PANREAC) were used as starting materials. Homogeneous mixtures of these powders were prepared in the suitable proportion to produce CA_6 with several Fe^{3+}/Al^{3+}% substitution in the CA_6 lattice (up to 70%). The powders were mixed by attrition milling during half an hour in water media using ZrO_2 balls, dried under mechanical stirring and finally sieved at $< 63\ \mu m$.

The different compositions prepared are shown in Fig. 2, where the numbers represent the percentage of Fe^{3+}/Al^{3+} ion replacement, or percentage of CF_6 as has usually been used.

To study the reaction progress as a function of temperature, materials of each composition were fired in an electric furnace under air atmosphere, for 2 h at temperatures in the range of 900–1600°C.

From the different powder mixtures, green compacts were obtained by cold isostatic pressing at 200 MPa. The obtained green compacts were fired in air in the temperature range showed in Table 1. The physical–chemical properties and the microstructure of the sintered compacts were studied.

2.2 Characterisation

The crystalline phase identification was carried out by powder X-ray diffraction using a Siemens D5000 equipped with Cu anode and graphite secondary monocromator.

In order to determine the solid solution limit at 1400°C, samples of each composition where fired for 10 h at this temperature, cooled down, homogenised and refired. This procedure was repeated at least four times. The reaction progress was studied by XRD. The solid solution CA_6 limit was calculated by means of Vegard's law. This law considers a gradual change in the crystalline structure parameters of a material between the limits of the solid solution. In a previous study, Dayal and Glasser[11] used the progressive linear changes in interplanar

Table 1. Sintering temperatures of different compositions

	Composition								
Temp. (°C)	*0*	*5*	*10*	*20*	*30*	*40*	*50*	*60*	*70*
1350								+	+
1400								+	+
1450					+	+	+	+	+
1500				+	+	+	+		
1550			+	+	+	+	+		
1600	+	+	+	+					
1650	+	+	+						
1700	+	+							
1750	+								

spacing of [2,0,11] CA_6 peak to calculate the solid solution limit at 1330°C. The interplanar spacing change of the same peak was measured by powder XRD using a silicon internal standard.[33]

The apparent density of sintered samples was measured by the Archimedes method using distilled water. True density was measured on milled samples ($< 63\,\mu m$) in a Micromeritics 1305 He pycnometer. The apparent density values are given as percentage of true density.

The microstructure of the materials was studied by scanning electron microscopy (SEM) on polished and thermal etched samples and, in some cases, gold-coated surfaces. Gold coating was not necessary for samples with high iron content due to its high electrical conductivity. A ZEISS DSM 942 microscopy, with an Energy Dispersive X-ray microanalysts (EDX) Link Oxford was used.

3 Results and Discussion

3.1 Phase evolution

Table 2 shows the different phases present in the materials as a function of composition and firing temperature. XRD identification was complicated by the shifting of CA_6 and Fe_2O_3 peaks due to the introduction of Fe_2O_3 and Al_2O_3 in solid solution in CA_6 and Fe_2O_3, respectively, peaks overlapping, and poor precision of the CAF_2 PDF file. As can be observed in Table 2, before the formation of CA_6, CA and CA_2 appear as intermediate phases in all mixtures. Materials with iron oxide also show the formation of CAF_2, the only ternary phase in the CaO–Al_2O_3–Fe_2O_3 phase equilibrium diagram (Fig. 2). But the most remarkable effect of iron addition oxide is the lower temperature of CA_6 formation, which is between 1200 and 1400°C in the samples with Fe_2O_3, instead of 1400–1600°C in the sample without iron.

Compositions 50 and 60, at 1400°C, present CA_6, CAF_2 and Fe_2O_3, and in the case of composition 70, CA_6 is not present, leaving CAF_2 and Fe_2O_3 as stable phases. Looking at the isothermal section of the CaO–Al_2O_3–Fe_2O_3 phase equilibrium diagram at 1330°C (Fig. 3), it can be observed that compositions 60 and 70 lie outside the CA_{6ss} line. Composition 60 lies in the tie triangle CA_6–F–Ternary phase, explaining the presence of these three phases in this composition at 1400°C. Composition 70 lies in the binary area CAF_2 + F explaining the absence of CA_6 at 1400°C in the sample. At 1330°C, composition 50 lies on the CA_6 solid solution line. Taking into account the results of this investigation, it seems that a reduction in the solid solution limit takes place at temperatures higher than 1330°C, meaning that sample 50 lies in the tie triangle CA_6–F–CAF at 1400°C.

The CA_6 solid solution limit at 1400°C was calculated. Figure 4 shows the results of the present

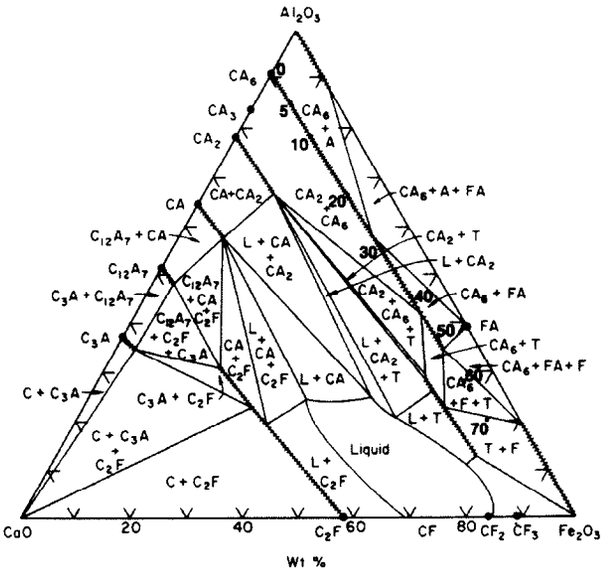

Fig. 3. Isothermal section of the CaO–$Al_2O_3Fe_2O_3$ phase diagram at 1330°C.

Table 2. Phases present as a function of composition and sintering temperature

	Composition								
Temp. (°C)	*0*	*5*	*10*	*20*	*30*	*40*	*50*	*60*	*70*
900	A + CA + CaO	A + F + CaO + CA	A + F + CA + CaO	F + A + A + CaO	F + A + CA + CaO	F + A + CA + CaO	F + A + CA + CAF_2	F + A + CA + CAF_2	A + F
1000	A + CA + CaO	A + CA + F	A + F + CA + CAF_2	A + F + CA + CAF_2	F + A + CA + CAF_2	F + A + CA + CAF_2	F + A + CA + CAF_2	F + A + CAF_2	F + A + CAF_2
1100	A + CA	A + CA_2 + CA + CAF_2	A + CA_2 + CAF_2 + F + CA	A + CA_2 + F + CAF_2	F + A + CA_2 + CAF_2	F + CAF_2 + A	F + CAF_2 + A	F + CAF_2 + A	F + CAF_2 + A
1200	A + CA_2 + CA	A + CA_2 + CA_6 + CAF_2	A + CA_2 + CAF_2 + CA_6 + F	A + CA_2 + CAF_2 + CA_6 + F	F + A + CAF_2 + CA_6	F + CAF_2 + A + CA_6	F + CAF_2 + A	F + CAF_2 + A	F + CAF_2 + A
1300	A + CA_2 + CA	A + CA_2 + CA_6	A + CA_2 + CA_6	CA_6 + A + CAF_2 + CA_2	CA_6 + CAF_2 + F	CA_6 + F + CAF_2	CA_6 + F + CAF_2	F + CAF_2 + CA_6	F + CAF_2
1400	A + CA_2 + CA_6	A + CA_2 + CA_6	CA_6 + A + CA_2	CA_6	CA_6	CA_6	CA_6 + F + CAF_2	CA_6 + F + CAF_2	F + CAF_2
1500	CA_6 + A + CA_2	CA_6 + A + CA_2	CA_6						
1600	CA_6	CA_6	CA_6						

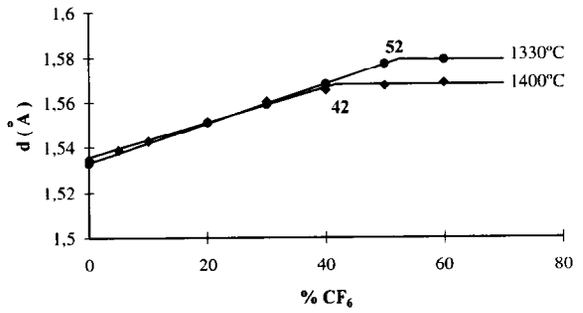

Fig. 4. Change in the CA_6[2,0,11] interplanar spacing at 1330°C[11] and 1400°C (present study) as a function of temperature.

investigation together with the ones obtained by Dayal and Glasser at 1330°C. Both lines have basically the same slope. The solid solution limit at 1400°C was found to be the composition with 42% of CF_6. This result explains the appearance of phases other than CA_6 in composition 50 at this temperature.

3.2 Density

Figure 5 shows the evolution of apparent density with firing temperature and composition of compacts fired for 5 h.

The highest density (96.5%) was obtained in the case of the sample without Fe_2O_3 for a sintering temperature of 1750°C. Up to composition 20, density increases with sintering temperature. For higher Fe_2O_3 contents, density increases up to a maximum before a decrease due to the appearance of glassy phase. The maximum apparent density of all materials varies from 92 to 97%, showing a slight decrease as iron content increases.

It can be pointed out that the addition of Fe_2O_3 enhances sintering. Looking, for example, at composition 20, it is possible to obtain the same density as sample 0 but at a sintering temperature 200°C lower, that is to say, it is possible to reduce the sintering temperature from 1750 to 1550°C.

3.3 Microstructure

Using the solid solution limit data obtained in this investigation as well as the results available in the literature, the vertical section of the CaO–Al_2O_3–Fe_2O_3 system through the CA_6–CF_6 line was drawn (Fig. 6). This section is of great importance in order to understand the microstructural evolution of calcium hexaluminate as a function of composition and firing temperature. Six different microstructures were found corresponding to different sintering areas of the mentioned section:

- Samples with low and medium iron content, fired at low temperatures (zone 1 in Fig. 6) present a microstructure composed of plate-like grains of CA_6 with big triangular pores (Fig. 7). These materials have low densities as it can be observed in Fig. 5.
- Samples with low iron content and higher firing temperature (zone 2 in Fig. 6) show a more equiaxed microstructure (Fig. 8). This change in morphology is followed by an increase of density.
- As can be observed in Fig. 6, for low amounts of Fe_2O_3 and very high temperatures, CA_6 and Al_2O_3 coexist with a liquid phase (zone 3). The microstructure of materials fired in such areas is composed of CA_6 plates with equiaxial

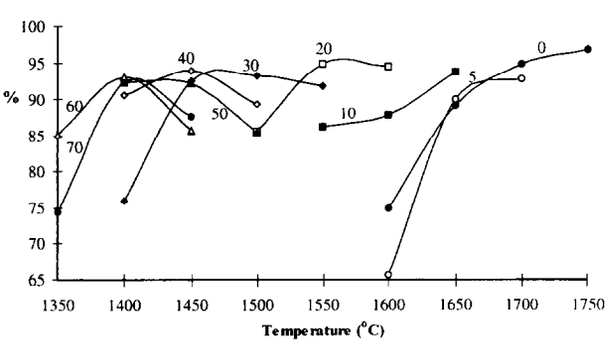

Fig. 5. Apparent density (% of real density) as a function of composition and firing temperature.

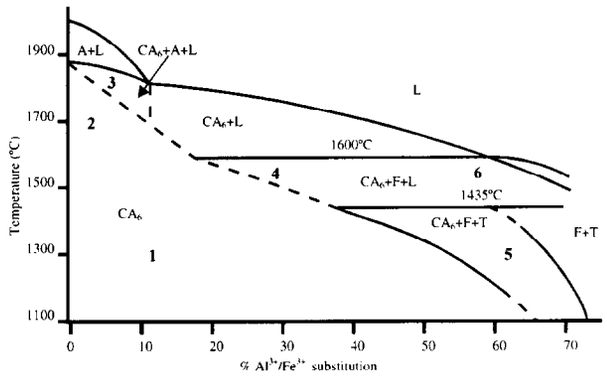

Fig. 6. Isoplethal section CaO–Al_2O_3–Fe_2O_3 phase diagram through the CA_6-CF_6 line.

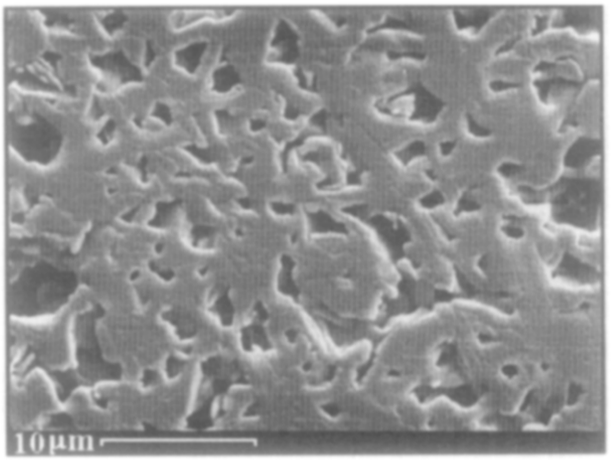

Fig. 7. Microstructure of compositions with low and medium Fe_2O_3 content at low temperatures.

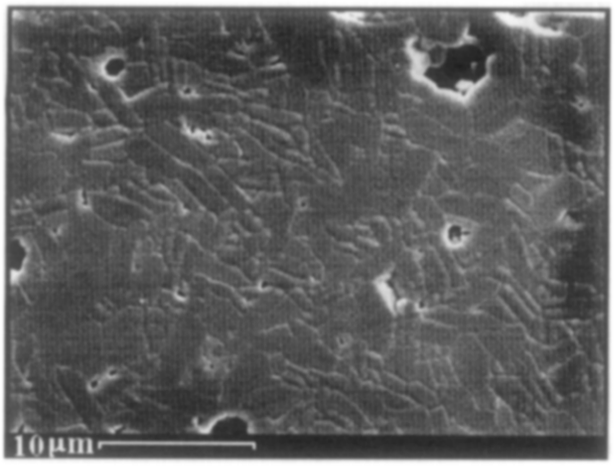

Fig. 8. Microstructure of compositions with low Fe_2O_3 content at high temperatures.

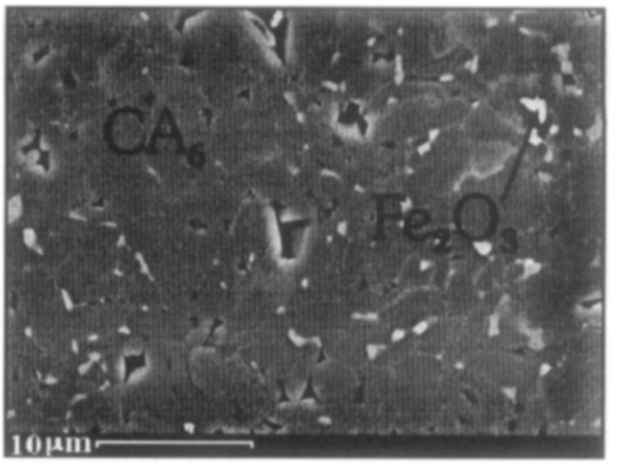

Fig. 10. Microstructure of compositions with medium Fe_2O_3 content at high temperatures.

Al_2O_3 grains between them (Fig. 9). In this microstructure, the piled up plates can be clearly observed. An increase of grain size is observed due to the presence of a glassy phase during sintering enhancing grain growth.

- Compositions 20 and 30 sintered at high temperatures, zone 4 in Fig. 6, show CA_6 equiaxed grains with small crystals of Fe_2O_3 between CA_6 grains (Fig. 10). That means that the solid solution limit has been exceeded. The amount of Fe_2O_3 particles is low and it cannot be observed by XRD.
- Samples 40–70 sintered at low temperatures (zone 5 in Fig. 6) show a microstructure composed by a random mixture of Fe_2O_3, CA_6 and CAF_2 grains (Fig. 11), as can be deduced from the isopletal section.
- At temperatures exceeding 1435°C (zone 6 in Fig. 6), the same three phases are present in a different arrangement. In Fig. 12 can be seen some CA_6 grains and big agglomerates of Fe_2O_3, surrounded by a matrix of CAF_2, CA_6 and small Fe_2O_3 grains. From Figs 2 and 6, it can be observed that 1435°C is the temperature of the invariant point CA_6–CAF_2–Fe_2O_3 and, when this temperature is achieved, a glassy phase appears. At higher temperatures, the glassy phase is in equilibrium with CA_6 and Fe_2O_3. As the grains of these two phases can grow in the presence of a considerable quantity of liquid, they show a large grain size. Small Fe_2O_3, CAF2 and CA_6 grains crystallise from the glassy phase upon cooling.

The different microstructures of these materials make them suitable for many applications:

- Materials with platelike grains and high porosity are suitable as catalytic supports for high temperatures, ceramic membranes and thermal shock resistant materials, for example.
- Equiaxed grains of CA_6 with small round pores are suitable as structural ceramics.
- Thanks to the different distribution of iron oxide grains, we can obtain a series of

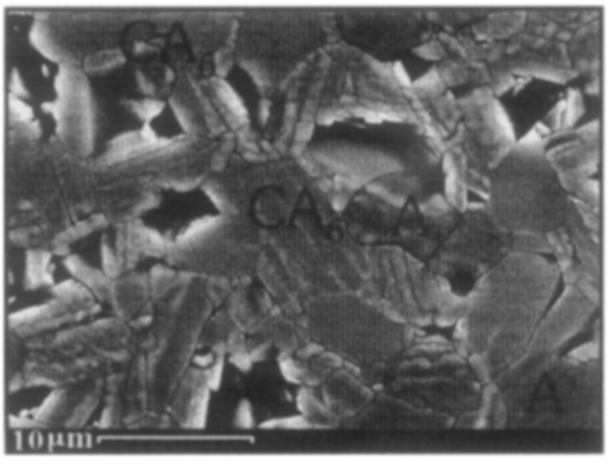

Fig. 9. Microstructure of compositions with low Fe_2O_3 content at very high temperatures.

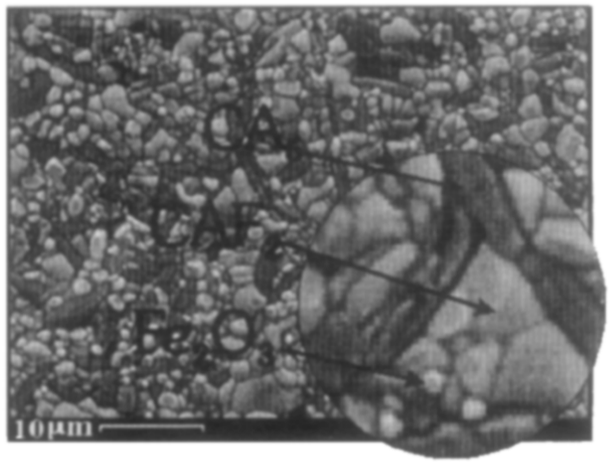

Fig. 11. Microstructure of compositions with high Fe_2O_3 content at temperatures lower than 1435°C.

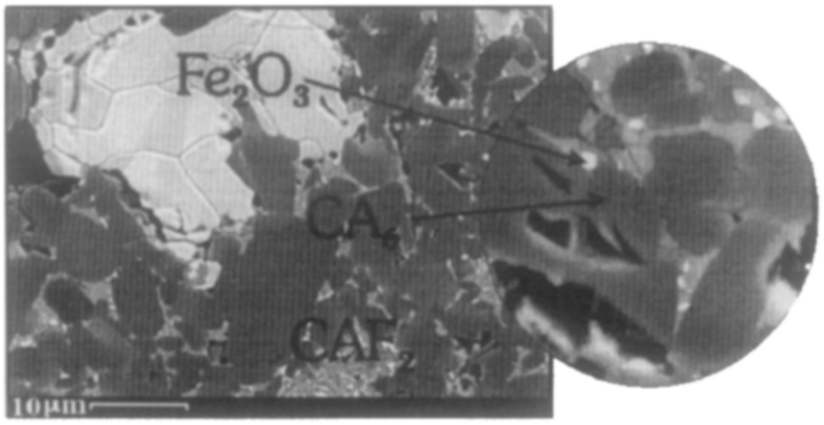

Fig. 12. Microstructure of compositions with high Fe_2O_3 content at temperatures higher than 1435°C.

materials with very different magnetic and electrical properties.

4 Conclusions

It was found that the phase evolution during the formation of the $CaO{\cdot}6(Al,Fe)_2O_3$ solid solution, with the appearance of several intermediate phases (CA, CA_2 and CAF_2) during, sintering and the final microstructures obtained, can be explained by means of the $CaO–Al_2O_3–Fe_2O_3$ phase equilibrium diagram.

The addition of Fe_2O_3 up to the solid solution limit enhances the formation and sintering of CA_6.

The solid solution limit at 1400°C is located at the composition with 42% Fe^{3+}/Al^{3+} atomic replacement.

Modifying Fe_2O_3 content and firing temperature, materials with different microstructures which are suitable for many applications can be obtained.

References

1. Kopanda, J. E. and Maczura, G., Production processes, properties, and applications for calcium aluminate cements. In *Alumina Chemical Science and Technology Handbook*, ed. L.D. Hart. American Ceramics Society, Westerville, OH, 1990, pp. 171–184.
2. Parker, K. M. and Sharp, J. H., Refractory calcium aluminate cements. *Trans. J. Br. Ceram. Soc.*, 1982, **8**(2), 35–42.
3. Schmid, H. and Jonghe, L. C., Structure and non-stoichiometry of calcium aluminates. *Philos. Mag. A.*, 1983, **48**(2), 287–297.
4. Utsunomiya, A., Tanaka, K., Morikawa, H., Marumo, F. and Kojima, H., Structure refinement of $CaO{\cdot}6Al_2O_3$. *J. Solid State Chem.*, 1988, **75**, 197–200.
5. Iyi, N., Takekawa, S. and Kimura, S., Crystal chemistry of hexaaluminates: β-Al_2O_3 and magnetoplumbite structures. *J. Solid State Chem.*, 1989, **83**(1), 8–19.
6. Park, J. G. and Cormack, A. N., Potential models for multicomponent oxides—Hexaaluminates. *Phil. Mag. B-Phys. Cond. Matter Struct. Elect. Opt. Magn. Prop.*, 1996, **73**(1), 21–31.
7. Criado, E., Pena, P. and Caballero, A., Influence of processing method on microstructural and mechanical properties of calcium hexaluminate compacts. *Science of Ceram.*, 1987, 193-8.T.
8. An, L. and Chan, H. M., Control of calcium hexaluminate grain morphology in in-situ toughened ceramic composites. *J. Mat. Science*, 1996, **31**, 3223–3229.
9. Cinibulk, M. K. and Hay, R. S., Textured magnetoplumbite fiber–matrix intherphase derived from sol-gel fiber coatings. *J. Am. Ceram. Soc.*, 1996, **79**(5), 1233–1246.
10. Burdese, A. and Brisi, C., Soluzioni solide ternarie tra calce allumina de ossido jerrico del tipo $CaO{\cdot}6(Al,Fe)_2O_3$. *Annali Chim.*, 1961, **41**, 564–568.
11. Dayal, R. R. and Glasser, F. P., Phase relations in the system $CaO–Al_2O_3–Fe_2O_3$. In *Science of Ceramics*, 1967, Vol 3, ed. G.H. Stewart. Academic Press, London, pp. 191–214.
12. Lister, D. H. and Glasser, F. P., Phase relations in the system $CaO–Al_2O_3$–iron oxide. *Trans Brit. Ceram. Soc.*, 1967, **66**(7), 293–305.
13. Imlach, J. A. and Glasser, F. P., Sub-solidus phase relations in the system $CaO–Al_2O_3–Fe–Fe_2O_3$. *Trans. J. Br. Ceram. Soc.*, 1971, **70**(6), 227–234.
14. Tak, J. B. and Young, D. J., Sulfur corrosion of calcium aluminate bonded castables. *Ceram. Bull.*, 1982, **61**(7), 725–727.
15. Brooksbank, D., Thermal expansion of calcium–aluminate inclusions and relation to tessellated stresses. *J. Iron Steel Inst.*, May 1970, 495–499.
16. Criado, E., de Aza, S. and Estrada, D. A., Caracteristicas dilatometricas de los aluminatos de calcio. *Bol. Soc. Esp. Ceram. Vidr.*, 1975, **14**(3), 271–273.
17. Criado, E., Estrada, D. A. and De Aza, S., Estudio dilatométrico sobre la formación de dialuminato y hexaaluminato de calcio en cementos y hormigones refractarios. *Bol. Soc. Esp. Ceram. Vidr.*, 1976, **15**(5), 319–321.
18. Nagaoka, T., Kanzani, S. and Yamaoka, Y., Mechanical properties of hot-pressed calcium hexaluminate ceramics. *J. Mat. Science Letters*, 1990, **9**, 219–221.
19. Mendoza, J. L., Freese, A. and Moore, R. E., Thermomechanical behaviour of calcium aluminate composites. *Adv. Refract. Technol., Ceram. Transac.*, 1990, **4**, 294–311.
20. Criado, E., Caballero, A. and Pena, P., Microstructural and mechanical properties of alumina–calcium hexaaluminate composites. In *High Tech Ceramics*, ed. P. Vicenzini. Elsevier Science, Amsterdam, 1987, pp. 2279–2289.
21. An, L., Chan, H. M., Padture, N. P. and Lawn, B. R., Damage-resistant alumina-based layer composites. *J. Mater. Res.*, 1996, **11**(1), 204–210.

22. An, L. and Chan, H. M., R-curve behavior of in-situ-toughened Al_2O_3:$CaAl_{12}O_{19}$ ceramic composites. *J. Am. Ceram. Soc.*, 1996, **79**(12), 3142–3148.
23. Cinibulk, M. K., Microstructure and mechanical behavior of an hibonite interphase in alumina-based composites. *Ceram. Eng. and Sci. Proceedings 165*, Sept–Oct 1995, pp. 633–641.
24. Cinibulk, M. K., Magnetoplumbite compounds as a fiber coating in oxide–oxide composites. *Ceram. Eng. and Sci. Proceedings*, **15**(5), Sept–Oct 1994, pp. 721–728.
25. Hench, L. L., Clark, D. E. and Harker, A. B., Review nuclear waste solids. *J. Mat. Sci.*, 1986, **21**, 1457–1478.
26. Morgan, P. E. D. and Cirlin, E. H., The magnetoplumbite crystal structure as a radwaste host. *J. Am. Ceram. Soc.*, 1982, **65**(7), C114–C115.
27. Morgan, P. E. D., Clarke, D. R., Jantzen, C. M. and Harker, A. B., High-alumina tailored nuclear waste ceramics. *J. Am. Ceram. Soc.*, 1981, **64**(5), 249–258.
28. Thery, V. and Lejus, C., Les Composes de type Magnetoplumbite et SLNA, Matériaux pour le stockage d'Elément Radioactifs? *Annales de Chimie-Science des Matériaux*, 1985, **4**, 397–399.
29. Kulkarni, D. K. and Prakash, C. S., Structural and magnetic properties of $CaAl_4Fe_8O_{19}$. *Bull. Mater. Sci.*, 1994, **17**(1), 35–39.
30. Prakash, C. S., Nanoti, V. M., Kulkarni, D. K. and Rao, G. M., Substitutional effect of magnetic behaviour in calcium hexaferrite. *J. Magnetism Magnetic Mat.*, 1995, **140**, 2089–2090.
31. Prakash, C. S., Nanoti, V. M. and Kulkarni, D. K., Magnetic characterisation of substituted calcium hexaferrite. *Mat. Letters*, 1995, **24**(P3), 171–173.
32. Floyd, J. R., Effect of secondary crystalline phases on dielectric losses in high-alumina bodies. *J. Am. Ceram. Soc.*, 1964, **47**(11), 539–543.
33. Wong-Ng, W. and Hubbard, C. R., Standard reference materials for X-ray diffraction. Part II. Calibration using d-spacing standards. *Powder Diffraction*, 1987, **2**(4), 242–248.